Received 19 March 2025; revised 20 April 2025; accepted 24 April 2025. Date of publication 2 May 2025; date of current version 20 May 2025.

Digital Object Identifier 10.1109/OJCOMS.2025.3566114

Intra-Symbol Differential Amplitude Shift Keying-Aided Blind Detector for Ambient Backscatter Communication Systems

SHUAIJUN MA[1], PENG WEI[1] (Member, IEEE), SA XIAO[1], JIANQUAN WANG[1], WANBIN TANG[1], AND WEI XIANG[2,3] (Senior Member, IEEE)

[1]National Key Laboratory of Wireless Communications, University of Electronic Science and Technology of China, Chengdu 611731, China
[2]School of Computing, Engineering and Mathematical Sciences, La Trobe University, Melbourne, VIC 3086, Australia
[3]College of Science and Engineering, James Cook University, Cairns, QLD 4870, Australia

CORRESPONDING AUTHORS: P. WEI AND S. XIAO (e-mail: wppisces@uestc.edu.cn; xiaosa@uestc.edu.cn)

This work was supported in part by the National Natural Science Foundation of China under Grant 62001094 and Grant 62301117, and in part by the China Postdoctoral Science Foundation under Grant 2020M683290.

ABSTRACT Ambient backscatter communications (AmBC) are a promising technology for addressing the energy consumption challenge in wireless communications through the reflection or absorption of surrounding radio frequency (RF) signals. However, it grapples with the intricacies of ambient RF signal and the round-trip path loss. For traditional detectors, the incorporation of pilot sequences results in a reduction in spectral efficiency. Furthermore, traditional energy-based detectors are inherently susceptible to a notable error floor issue, attributed to the co-channel direct link interference (DLI). Consequently, this paper proposes a blind symbol detector without the prior knowledge of the channel state information, signal variance, and noise variance. By leveraging the intra-symbol differential amplitude shift keying (IDASK) scheme, this detector effectively redirects the majority of the DLI energy towards the largest eigenvalue of the received sample covariance matrix, thereby utilizing the second largest eigenvalue for efficient symbol detection. In addition, this paper conducts theoretical performance analyses of the proposed detector in terms of the false alarm probability, missed detection probability, and the bit-error rate (BER) lower bound. Simulation results demonstrate that the proposed blind detector exhibits a significant enhancement in symbol detection performance compared to its traditional counterparts.

INDEX TERMS Ambient backscatter communications, Blind symbol detector, Intra-symbol differential amplitude shift keying.

I. INTRODUCTION

RECENTLY, ambient backscatter communications (AmBC) have emerged as an energy-efficient technology to satisfy the low-power radio frequency (RF) requirements in green Internet of Things (IoT) [1], [2]. Unlike traditional communication system of generating RF signal for information transmission, an AmBC system uses backscatter devices (BDs) to reflect surrounding RF signals to the receiver [3], [4], [5]. In addition, it can achieve high spectral utilization efficiency by sharing the same spectra with traditional communication systems [6], [7], [8]. However, the signal reflected through the transmitter-BD-receiver link in the AmBC system is invariably affected by the direct link interference (DLI) from an ambient RF source. Thus, successful symbol detection in the AmBC system necessitates the estimation of: (i) the direct channel from the RF source to the corresponding receiver; and (ii) the cascaded channel in the source-BD-receiver link. Nonetheless, the path loss of the cascaded channel is much higher than that of the direct channel [9], which presents a formidable challenge in detecting backscatter symbols.

Numerous traditional detectors have been developed for AmBC systems [10], [11], [12], [13], [14], [15], [16], [17], [18], [19], [20], [21], [22], [23], [24], [25]. In the traditional detectors, symbols are evaluated based on the statistical properties of the received signal. According to whether the

detector possesses complete knowledge of ambient RF signal and channel state information (CSI), traditional detectors can be categorized into coherent detectors and non-coherent detectors [26].

A coherent detector leverages prior knowledge by utilizing comprehensive ambient signal information and CSI for symbol detection. Based on this, the authors of [10] proposed the maximum a posterior probability (MAP) detector and the energy-threshold determination (ETD) detector for a multi-antenna AmBC system with M-ary frequency shift keying (MFSK) modulation. These detectors effectively counter jammer attacking. Reference [12] designed the MAP detector for AmBC system using on-off keying (OOK) modulation to achieve an error-floor-free detection performance. In [11], an adaptive dual-threshold detector was proposed for frequency diverse array based AmBC systems. Reference [8] derived the optimal maximum-likelihood (ML) detector, sub-optimal linear detectors as well as successive interference-cancellation (SIC) based detectors for the AmBC system with flat fading channels.

Non-coherent detectors operate without requiring full knowledge of the ambient signal and complete CSI. The authors of [19] proposed ML and energy-based detectors, which utilize incomplete CSI for the AmBC system with Gaussian signals and phase shift keying (PSK) signals. Reference [20] proposed the generalized likelihood ratio test (GLRT) detector for AmBC system without the knowledge of CSI. To further enhance the detection performance in AmBC systems, the authors of [21] proposed a multi-antenna AmBC signal detector based on the maximum-eigenvalue of the received signal covariance matrix. This detector employed pilot sequences to estimate the statistical variances of the received signals. Reference [22] proposed an energy-based AmBC detector for complex RF signals including complex-valued Gaussian or phase shift keying (PSK) signals, and designed the statistical variances estimator of the received signals. Reference [23] proposed an efficient detector with interleaved coding and pilot sequences, which utilizes the complex ratio to preserve the phase information. Additionally, the authors of [24] employed the eigenvalue decomposition of the received signal covariance matrix for CSI estimation. Reference [25] designed a CSI estimator based on a clustering method with pilot sequences.

Nonetheless, the incorporation of pilot sequences results in a reduction in spectral efficiency. To address this issue, the authors of [13], [14], [15] employed the differential encoders in the BD of the AmBC systems. Specifically, in [13], the authors proposed an energy-aware detector and provided an analytical characterization of its achievable bit error rate (BER) performance. In [14], a data-driven estimator was designed to efficiently evaluate the statistical variances of the received signals to enhance the symbol detection performance. In [15], an improved detector was developed to eliminate the assumption of equal probability for symbol bits. This improvement also removes the need for an estimation process, simplifying the detection mechanism. In addition, [18] proposed the expectation maximization (EM) based blind CSI estimator for the AmBC system with PSK ambient signals. The EM-based signal detection method was further developed in [16], [17]. Specifically, in [17], the authors proposed three detectors for the AmBC system with multi-antenna BD, and the latter two are blind detectors. Additionally, they proposed optimal tag antenna selection schemes to improve the detection performance. In [16], the authors proposed an AmBC system with multiple BDs, and a non-coherent parallel detection algorithm was designed to detect the symbols without requiring CSI. However, these detectors often exhibit a high error floor.

Given the above observations, one of the most significant challenges in AmBC systems is to mitigate the high DLI in a completely blind detection manner. To tackle this challenge, we design a blind symbol detector for AmBC systems. The proposed detector leverages the eigenvalues of the received signal covariance matrix as a key feature for detection. Intuitively, with IDASK-modulated transmission and multi-antenna reception, the largest eigenvalue primarily corresponds to the dominant DLI component, while the second largest eigenvalue captures the contribution of the backscatter signal. By focusing on the second largest eigenvalue, the proposed detector effectively isolates the backscatter signal from the strong DLI, enabling the AmBC signal detection without the prior knowledge of the ambient RF signal and CSI. Our main contributions of this paper can be summarized as follows.

- Firstly, we propose a blind symbol detector for the AmBC system based on the second largest eigenvalue of the received signal covariance matrix. In the AmBC system, the intra-symbol differential amplitude shift keying (IDASK) is employed to mitigate the DLI. Furthermore, we design a noise variance estimator based on the impact of the received signal on the second largest eigenvalue, in order to improve the estimation accuracy.
- Secondly, we derive the close-form expressions of the missed detection probability and false alarm probability of the proposed blind detector. Furthermore, we evaluate a lower BER bound using the total variation theory.
- Finally, simulation results demonstrate that the proposed detector exhibits superior detection performance in AmBC systems compared to conventional counterparts.

The rest of the paper is organized as follows. In Section II, we introduce the AmBC system model with a single-antenna ambient source, an IDASK-based BD, and a multi-antenna receiver. In Section III, the blind symbol detector based on the second largest eigenvalue is presented. In Section IV, the theoretical missed detection probability and false alarm probability of the proposed blind detector are analyzed, followed by the analysis of the lower bound of BER. In Section V, simulation experiments are given. In Section VI, this paper is concluded.

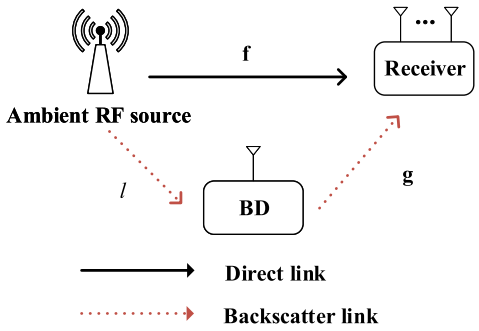

FIGURE 1. An AmBC system with a single-antenna ambient RF source, a single-antenna BD, and a multi-antenna receiver.

Throughout this paper, lowercase symbols represent scalars, while boldface symbols denote vectors or matrices. $\mathcal{CN}(\mu, \sigma^2)$ refers to the circularly symmetric complex Gaussian distribution with mean μ and variance σ^2, whereas the real Gaussian distribution with mean μ and variance σ^2 is denoted by $\mathcal{N}(\mu, \sigma^2)$. $\mathbf{I}_N$ stands for the identity matrix of order N. $\mathbf{S}^H$, tr($\mathbf{S}$), rank($\mathbf{S}$) and det($\mathbf{S}$) represent the conjugate transpose, trace, rank and determinant of the matrix $\mathbf{S}$, respectively. $\|\mathbf{w}\|$ denotes the Euclidean norm of the vector $\mathbf{w}$. $\mathbf{C}^{M\times N}$ represents a complex matrix with M rows and N columns. $\exp(\cdot)$ is the exponential function. $\mathcal{Q}(\cdot)$ denotes the Q-function. $\mathbb{Z}$ stands for the set of integers.

II. SYSTEM MODEL

This paper delineates a three-node AmBC system comprising a single-antenna ambient RF source, a single-antenna backscatter device (BD), and a receiver equipped with M antennas. The BD has an analogue front-end that can use the power switching protocol for energy harvesting and information transmission [26]. As illustrated in Fig. 1, the ambient source broadcasts its RF signal via an omnidirectional antenna. The BD is designed to modulate its binary symbols over the incident RF signal from the ambient source by manipulating its antenna impedance. Subsequently, the BD reflects the incident RF signal to the receiver based on the bit information. At the receiver, rather than demodulating the ambient signal directly, our objective is to detect the information embedded by the BD. In this paper, we refer to the direct communication link between the ambient source and receiver as the direct link, and the cascade link between the ambient source (after passing BD) and the receiver as the backscatter link.

It is noted that when a multi-antenna RF source is considered, beamforming techniques are typically employed to direct the RF transmission. In such scenarios, the BD must be placed within a specific region to ensure it can effectively receive the ambient RF signal and modulate it. For simplicity, our system model assumes an omnidirectional antenna at the ambient source to relax the strict placement requirements for the BD. Additionally, while a multi-antenna BD could be incorporated into our system model, this would introduce increased complexity and high costs [17]. Therefore, we assume that the BD is equipped with a single antenna.

A. IDASK-AIDED SIGNAL TRANSMISSION

The energy of the reflected RF signal in the backscatter link is lower than that of the direct link. Thus, to capture the low-energy reflected RF signal, the BD has a lower rate than the ambient source [25]. As illustrated in Fig. 2, we assume that the period of one BD symbol is equal to that of N consecutive symbols in the ambient source.

We first assume that the channels exhibit quasi-static block-fading characteristics. Thus, according to [23], via a short-distance communication link connecting the ambient source and the BD, the RF signal $\bar{s}_n$ received at the BD can be written as

$$\bar{s}_n = A_l l s_n, \tag{1}$$

where $n = 1, \ldots, N$ and s_n denotes the signal transmitted by the ambient source at time interval n with variance σ_s^2. A_l and l denote the large-scale and small-scale channel fading of the source-BD link, respectively [23], [25].

To modulate its information into the ambient RF signal while mitigating the high DLI, the BD employs IDASK. Unlike traditional ASK, IDASK introduces a differential encoding mechanism in a single BD symbol period. Specifically, the amplitude levels of adjacent signal segments in the same BD symbol are compared, and the bit information is embedded in the relative amplitude changes rather than absolute values. We assume that the binary variables $b_n = 1$ and $b_n = 0$ denote the reflection and non-reflection states of BD, respectively. Based on IDASK, the BD modulates the binary symbol $c \in \{0, 1\}$ into the ambient RF signal by leveraging the two states of reflecting and non-reflecting its received RF signal $\bar{s}_n$. For $c = 0$, the BD remains in the non-reflection state during one BD symbol, that is, $b_n = 0$ for all $n = 1, 2, \ldots, N$. On the contrary, for $c = 1$, as depicted in Fig. 2, only a portion of the received RF signal in one BD symbol period is reflected. In this paper, the RF signal is not reflected in the first $(1-k)N$ symbol periods of the ambient source, meaning $b_n = 0$ for $n = 1, 2, \ldots, (1-k)N$, and is reflected in the last kN symbol periods of the ambient source, where $b_n = 1$ for $n = 1 + (1-k)N, \ldots, N$. The parameter k represents the reflection ratio of the RF signal during one BD symbol period, with $kN \in \mathbb{Z}$ and $k \in (0, 1]$. Therefore, the state of BD during one symbol period should satisfy

$$b_n = \begin{cases} 0, & n = 1, \ldots, N, c = 0, \\ & \text{or } n = 1, \ldots, (1-k)N, c = 1, \\ 1, & n = (1-k)N + 1, \ldots, N, c = 1. \end{cases} \tag{2}$$

Consequently, the RF signal reflected by BD can be expressed as

$$s_n^t = \alpha b_n \bar{s}_n, \tag{3}$$

where α denotes the reflection coefficient of BD [25].

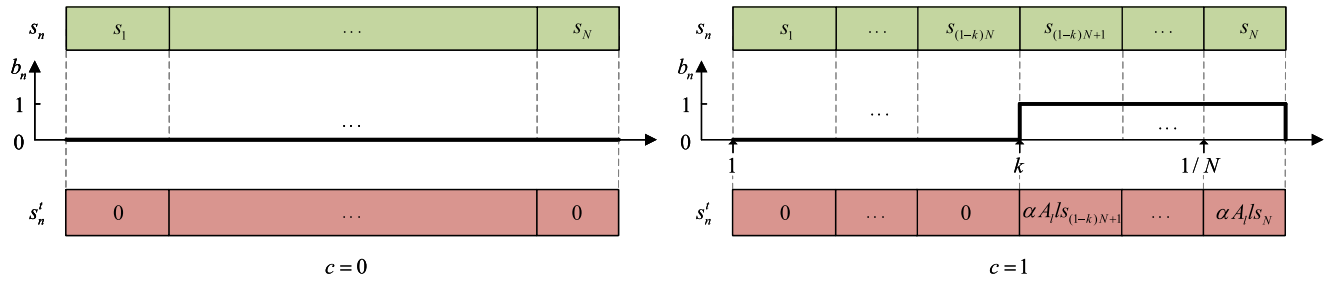

FIGURE 2. Schematic diagram of the IDASK scheme.

B. RECEIVED AMBC SIGNAL

According to [15], under the assumption of a short distance between the BD and receiver, the propagation delays of the direct and backscatter links are approximately equal. Consequently, the received RF signal is expressed as

$$\mathbf{y}_n = A_f \mathbf{f} s_n + A_g \mathbf{g} s_n^t + \mathbf{u}_n = \mathbf{y}_n^b + \mathbf{y}_n^d + \mathbf{u}_n, \tag{4}$$

where A_g and $\mathbf{g} \in \mathbf{C}^{M\times 1}$ denote the large-scale and small-scale channel fading of the BD-receiver link, respectively. A_f and $\mathbf{f} \in \mathbf{C}^{M\times 1}$ denote the large-scale channel gain and the small-scale channel fading vector of the direct link, respectively [23], [25]. We assume $h_1 = A_f \mathbf{f}$ and $h_2 = \alpha A_l l A_g g$. Thus, we have $\mathbf{y}_n^b = b_n \mathbf{h}_2 s_n$ and $\mathbf{y}_n^d = \mathbf{h}_1 s_n$. In addition, $\mathbf{u}_n \sim \mathcal{CN}(0, \sigma_n^2 \mathbf{I}_M)$ is the additive white Gaussian noise (AWGN) with variance σ_n^2.

The hypotheses of BD sending symbols $c = 0$ and $c = 1$ are denoted by $\mathcal{H}_0$ and $\mathcal{H}_1$, respectively. The received RF signal $\mathbf{y}_n$ is expressed in matrix form as $\mathbf{Y} = [\mathbf{Y}_0, \mathbf{Y}_1] \in \mathbf{C}^{M\times N}$, where $\mathbf{Y}_0 = [\mathbf{y}_1, \mathbf{y}_2, \ldots, \mathbf{y}_{(1-k)N}] \in \mathbf{C}^{M\times(1-k)N}$ and $\mathbf{Y}_1 = [\mathbf{y}_{(1-k)N+1}, \mathbf{y}_{(1-k)N+2}, \ldots, \mathbf{y}_N] \in \mathbf{C}^{M\times(kN)}$. The signal s_n could be either a complex Gaussian signal or a modulated one [26]. According to [26], a complex Gaussian ambient source is assumed, which satisfies $\mathbf{s}_n \sim \mathcal{CN}(0, \sigma_s^2)$. Then, under the hypothesis of $\mathcal{H}_i$, $\mathbf{Y}_j \sim \mathcal{CN}(0, \mathbf{R}_i^j)$, where $i, j \in \{0, 1\}$, and we have

$$\mathbf{R}_0^0 = \mathbb{E}\Big[\mathbf{Y}_0 \mathbf{Y}_0^H | \mathcal{H}_0\Big] = \sigma_s^2 \mathbf{h}_1 \mathbf{h}_1^H + \sigma_n^2 \mathbf{I}_M = \mathbf{R}_1^0 = \mathbf{R}_0^1, \tag{5}$$

$$\mathbf{R}_1^1 = \mathbb{E}\Big[\mathbf{Y}_1 \mathbf{Y}_1^H | \mathcal{H}_1\Big] = \sigma_s^2 (\mathbf{h}_1 + \mathbf{h}_2)(\mathbf{h}_1 + \mathbf{h}_2)^H + \sigma_n^2 \mathbf{I}_M. \tag{6}$$

Then, the AmBC symbol detection process follows the binary hypothesis test as

$$\mathbf{Y} = [\mathbf{Y}_0, \mathbf{Y}_1] \sim \begin{cases} \mathcal{CN}(0, \mathbf{R}_0^0) \cdot \mathcal{CN}(0, \mathbf{R}_0^1), & \mathcal{H}_0, \\ \mathcal{CN}(0, \mathbf{R}_1^0) \cdot \mathcal{CN}(0, \mathbf{R}_1^1), & \mathcal{H}_1. \end{cases} \tag{7}$$

Based on [27], under the hypothesis of $\mathcal{H}_i$, the probability density function (PDF) of $\mathbf{Y}_j$ can be formulated as

$$f(\mathbf{Y}_j; \mathcal{H}_i) = \frac{\exp\left\{-\mathrm{tr}\left(\left(\mathbf{R}_i^j\right)^{-1} \mathbf{Y}_j \mathbf{Y}_j^H\right)\right\}}{\pi^{MN} \det\left(\mathbf{R}_i^j\right)^{N_j}}, \tag{8}$$

where $N_0 = (1-k)N$ and $N_1 = kN$. Based on (8), the PDF of $\mathbf{Y}$ can be derived as

$$\begin{aligned} f(\mathbf{Y}; \mathcal{H}_0) &= f(\mathbf{Y}_0; \mathcal{H}_0) \cdot f(\mathbf{Y}_1; \mathcal{H}_0) \\ &= \frac{\exp\left\{-\mathrm{tr}\left(\left(\mathbf{R}_0^0\right)^{-1} \mathbf{Y}\mathbf{Y}^H\right)\right\}}{\pi^{MN} \det\left(\mathbf{R}_0^0\right)^N}, \end{aligned} \tag{9}$$

$$f(\mathbf{Y}; \mathcal{H}_1) = \frac{\exp\left\{-\mathrm{tr}\left(\left(\mathbf{R}_1^0\right)^{-1} \mathbf{Y}_0 \mathbf{Y}_0^H + \left(\mathbf{R}_1^1\right)^{-1} \mathbf{Y}_1 \mathbf{Y}_1^H\right)\right\}}{\pi^{MN} \det\left(\mathbf{R}_1^0\right)^{N_0} \det\left(\mathbf{R}_1^1\right)^{N_1}}. \tag{10}$$

Under the assumption of equal probabilities of symbols $c = 0$ and $c = 1$, according to [12], the general likelihood ratio test (GLRT) is utilized to detect the symbols as follows

$$\begin{aligned} L(\mathbf{Y}) &= \frac{f(\mathbf{Y}; \mathcal{H}_1)}{f(\mathbf{Y}; \mathcal{H}_0)} \\ &= \frac{\exp\left\{-\mathrm{tr}\left(\left(\mathbf{R}_1^1\right)^{-1} \mathbf{Y}_1 \mathbf{Y}_1^H\right)\right\} \det\left(\mathbf{R}_0^1\right)^{N_1}}{\exp\left\{-\mathrm{tr}\left(\left(\mathbf{R}_0^1\right)^{-1} \mathbf{Y}_1 \mathbf{Y}_1^H\right)\right\} \det\left(\mathbf{R}_1^1\right)^{N_1}} \\ &\underset{\mathcal{H}_0}{\overset{\mathcal{H}_1}{\gtrless}} 1. \end{aligned} \tag{11}$$

In practice, the complete information of the ambient RF signal variance, noise variance, and the CSI is unavailable. As a result, the GLRT-based detector cannot achieve the optimal symbol detection performance [26]. Furthermore, in practical AmBC communication systems, the cascaded channel gain is considerably lower than the direct channel gain [25]. Here, we define an average energy ratio $\Delta\gamma$ of the cascaded channel gain to the direct channel gain as follows

$$\Delta\gamma = \frac{\mathbb{E}\left[\|\mathbf{h}_2\|^2\right]}{\mathbb{E}\left[\|\mathbf{h}_1\|^2\right]}. \tag{12}$$

As the value of $\Delta\gamma$ is close to zero, the direct link will result in significant interference to the backscatter link. To solve this problem, in the next section, we will propose a blind symbol detector based on the second largest eigenvalue of the received signal covariance matrix.

III. SECOND LARGEST EIGENVALUE BASED BLIND DETECTOR

In this section, we first design a blind detector based on the second largest eigenvalue of the covariance matrix of

the received AmBC signal. Subsequently, a noise variance estimation algorithm is proposed.

A. BLIND SYMBOL DETECTOR

Based on (5) and (6), the covariance matrix of the received AmBC signal can be written as

$$\begin{aligned}\mathbf{R}_i &= \mathbb{E}\Big[\mathbf{Y}\mathbf{Y}^H|\mathcal{H}_i\Big] \\ &= k\mathbb{E}\Big[\mathbf{Y}_1\mathbf{Y}_1^H|\mathcal{H}_i\Big] + (1-k)\mathbb{E}\Big[\mathbf{Y}_0\mathbf{Y}_0^H|\mathcal{H}_i\Big]. \end{aligned} \tag{13}$$

For hypotheses of $\mathcal{H}_1$ and $\mathcal{H}_0$, Eq. (13) is respectively expanded as

$$\mathbf{R}_1 = (1-k)\sigma_s^2\mathbf{h}_1\mathbf{h}_1^H + k\sigma_s^2(\mathbf{h}_1+\mathbf{h}_2)(\mathbf{h}_1+\mathbf{h}_2)^H + \sigma_n^2\mathbf{I}_M, \tag{14}$$

$$\mathbf{R}_0 = \sigma_s^2\mathbf{h}_1\mathbf{h}_1^H + \sigma_n^2\mathbf{I}_M. \tag{15}$$

Under hypothesis $\mathcal{H}_1$, we derive the following theorem on $\mathbf{R}_1$.

Theorem 1: When $\Delta\gamma \to 0$, the determinant of $\mathbf{R}_1$ can be approximated as follows

$$\begin{aligned}\det(\mathbf{R}_1) \approx &\left(\sigma_s^2\|\mathbf{h}_1\|^2 + \sigma_n^2\right)\left(\left(k-k^2\right)\sigma_s^2\|\mathbf{h}_2\|^2 + \sigma_n^2\right) \\ &\cdot(\sigma_n^2)^{M-2}. \end{aligned} \tag{16}$$

Proof: See Appendix-A. ■

Without loss of generality, we assume that $l_1 \geq l_2 \geq \cdots \geq l_M$ are the ordered eigenvalues of $\mathbf{R}_1$, and $\lambda_1 \geq \lambda_2 \geq \cdots \geq \lambda_M$ are the generalized eigenvalues of the sample covariance matrix $\hat{\mathbf{R}}$, where $\hat{\mathbf{R}}$ is expressed as

$$\hat{\mathbf{R}} = \frac{\mathbf{Y}\mathbf{Y}^H}{N}. \tag{17}$$

As $\Delta\gamma$ approaches zero, according to Theorem 1, we have

$$l_1 = \sigma_s^2\|\mathbf{h}_1\|^2 + \sigma_n^2, \tag{18}$$

$$l_2 = \sigma_s^2\|\mathbf{h}_2\|^2\left(k-k^2\right) + \sigma_n^2, \tag{19}$$

$$l_3 = \cdots = l_M = \sigma_n^2. \tag{20}$$

Eqs. (18)-(20) reveal that when $k < 1$, IDASK modulation combined with multi-antenna reception significantly enhances the separation of the backscatter signal from the received AmBC signal by redirecting the energy of the backscatter signal towards the second largest eigenvalue of $\mathbf{R}_1$. Thus, the DLI corresponding to the largest eigenvalue can be directly eliminated from the received AmBC signal. When $k = 1$, IDASK becomes the conventional OOK in [21]. In this case, the energy of the backscatter signal will be directed towards the largest eigenvalue of $\mathbf{R}_1$, combined with the DLI.

Under hypothesis $\mathcal{H}_0$, we have $\det(\mathbf{R}_0) = (\sigma_s^2\|\mathbf{h}_1\|^2 + \sigma_n^2)(\sigma_n^2)^{M-1}$ [27], and

$$l_1 = \sigma_s^2\|\mathbf{h}_1\|^2 + \sigma_n^2, \tag{21}$$

$$l_2 = \cdots = l_M = \sigma_n^2. \tag{22}$$

It can be seen that the second largest eigenvalue of $\mathbf{R}_0$ is only related to noise, while the left eigenvalues are identical to those obtained in hypothesis $\mathcal{H}_1$. Therefore, under hypotheses $\mathcal{H}_0$ and $\mathcal{H}_1$, the second largest eigenvalue of the covariance matrix of the received signal can be served as a key indicator for the detection of reflected signals through the BD. Based on this, we design the following detector

$$T(\mathbf{Y}) = \frac{\lambda_2}{\sigma_n^2} \underset{\mathcal{H}_0}{\overset{\mathcal{H}_1}{\gtrless}} \eta, \tag{23}$$

where η is a given threshold. To conduct the second largest eigenvalue-based symbol detection, the noise variance should be estimated in advance.

B. ESTIMATION OF NOISE VARIANCE

Under hypothesis $\mathcal{H}_0$, according to (22), the noise variance is estimated as

$$\hat{\sigma}_n^2 = \frac{\mathrm{tr}(\hat{\mathbf{R}}) - \lambda_1}{M-1}, \mathcal{H}_0. \tag{24}$$

Under hypothesis $\mathcal{H}_1$, according to (20), the noise variance can be estimated as

$$\hat{\sigma}_n^2 = \frac{\mathrm{tr}(\hat{\mathbf{R}}) - \lambda_1 - \lambda_2}{M-2}, \mathcal{H}_1. \tag{25}$$

It can be observed from (24) and (25) that due to the effect of the backscatter link, different expressions are used to estimate the noise variance. In practical blind detection, to accurately evaluate the noise variance, the reflection state of the BD should be first determined. Fortunately, considering the higher second largest value in the reflection state compared to the non-reflection state, $\lambda_2 - \lambda_m$ $(m = 3, 4, \ldots, M)$ will be small in hypothesis $\mathcal{H}_0$, and will be a larger value compared to the noise variance in hypothesis $\mathcal{H}_1$. Thus, the estimation of the noise variance is devised as

$$\hat{\sigma}_n^2 = \begin{cases} \dfrac{\mathrm{tr}(\hat{\mathbf{R}}) - \lambda_1}{M-1}, & \lambda_2 - \lambda_m < \dfrac{\mathrm{tr}(\hat{\mathbf{R}}) - \lambda_1 - \lambda_2}{M-2}, \\ \dfrac{\mathrm{tr}(\hat{\mathbf{R}}) - \lambda_1 - \lambda_2}{M-2}, & \lambda_2 - \lambda_m \geq \dfrac{\mathrm{tr}(\hat{\mathbf{R}}) - \lambda_1 - \lambda_2}{M-2}. \end{cases} \tag{26}$$

Consequently, based on (26), the blind detector in (23) is improved as

$$T(\mathbf{Y}) = \begin{cases} \dfrac{\lambda_2(M-1)}{\mathrm{tr}(\hat{\mathbf{R}}) - \lambda_1}, & \lambda_2 - \lambda_m < \dfrac{\mathrm{tr}(\hat{\mathbf{R}}) - \lambda_1 - \lambda_2}{M-2}, \\ \dfrac{\lambda_2(M-2)}{\mathrm{tr}(\hat{\mathbf{R}}) - \lambda_1 - \lambda_2}, & \lambda_2 - \lambda_m \geq \dfrac{\mathrm{tr}(\hat{\mathbf{R}}) - \lambda_1 - \lambda_2}{M-2}. \end{cases} \tag{27}$$

C. COMPUTATIONAL COMPLEXITY

The computational complexity of the proposed detector primarily involves two operations: (1) generating the sample covariance matrix $\hat{\mathbf{R}}$ and (2) extracting the eigenvalues of $\hat{\mathbf{R}}$. According to [27], the former requires M^2N multiplications

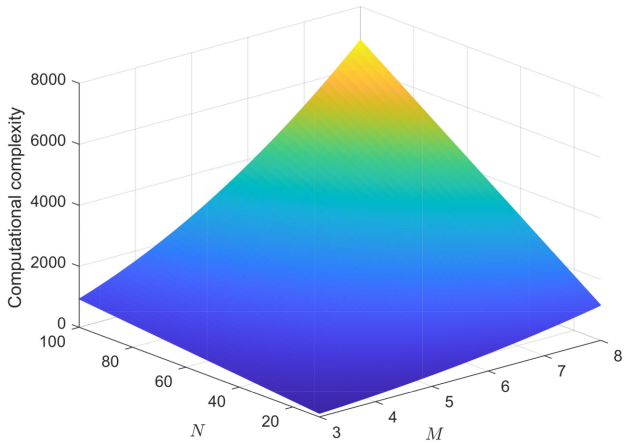

FIGURE 3. Computational complexity with varying values of M and N.

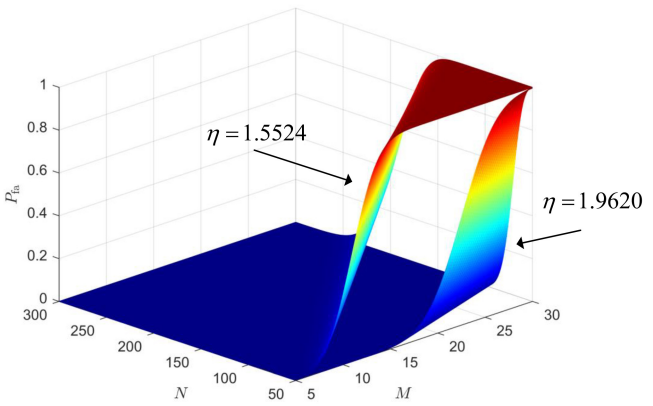

FIGURE 4. Analytical false alarm probability with varying values of M, N, and η, where $M = 5, 6, \ldots, 30$, $N = 50, 60, \ldots, 300$, and $\eta = 1.5524, 1.962$.

and $M^2(N-1)$ additions, while the later requires $\mathcal{O}(M^3)$ multiplications and $\mathcal{O}(M^3)$ additions. Thus, the total computational complexity is proportional to

$$\mathcal{O}\left(M^2N\right) + \mathcal{O}\left(M^3\right). \tag{28}$$

As shown in Fig. 3, the complexity of the proposed detector increases as M and N increase. Since $N \gg M$, this complexity mainly depends on N. Furthermore, in practice, since $N \gg M$, the complexity is dominated by $\mathcal{O}(M^2N)$. Since the number of antennas M at the receiver is typically small (e.g., $M = 4$ in many multiple-input multiple-output (MIMO) systems), the proposed method achieves a relatively low-complexity implementation, making it suitable for practical applications.

IV. ANALYTICAL PERFORMANCE EVALUATION

In this section, we evaluate the detection performance of the proposed blind detector in terms of the false alarm probability, the missed detection probability, and the lower bound of BER.

A. FALSE ALARM PROBABILITY

Under hypothesis $\mathcal{H}_0$, when threshold η is much lower than the value of λ_2/σ_n^2, the received AmBC signal is susceptible to being erroneously detected as a signal with the reflected RF signal, resulting in a false alarm. To quantify the impact of the threshold on the false alarm, we analyze the false alarm probability. Firstly, we define the ratio of the transmitted RF signal variance to the channel noise variance as $\gamma = \sigma_s^2/\sigma_n^2$. Then the following lemma is proposed to demonstrate the distribution of λ_2/σ_n^2.

Lemma 1: When γ is large, the second largest eigenvalue λ_2 normalized by σ_n^2 follows

$$\frac{\lambda_2/\sigma_n^2 - \mu_{N,M-1}}{\sigma_{N,M-1}} \sim TW_2, \tag{29}$$

where TW_2 denotes the Tracy-Widom distribution of order 2 [28], and

$$\mu_{N,M} = \left(1 + \sqrt{\frac{M}{N}}\right)^2, \tag{30}$$

$$\sigma_{N,M} = \frac{1}{\sqrt{N}}\left(1 + \sqrt{\frac{M}{N}}\right)\left(\frac{1}{\sqrt{N}} + \frac{1}{\sqrt{M}}\right)^{1/3}. \tag{31}$$

Proof: See Appendix-B. ■

According to Lemma 1, a closed-form expression for the false alarm probability is derived under the asymptotic regime where M and N are large.

Lemma 2: Under large M and N, the false alarm probability P_{fa} is written as

$$\begin{aligned} P_{\text{fa}} &= P[T(\mathbf{Y}) > \eta | \mathcal{H}_0] \\ &= P\left[\frac{\lambda_2/\sigma_n^2 - \mu_{N,M-1}}{\sigma_{N,M-1}} > \frac{\eta - \mu_{N,M-1}}{\sigma_{N,M-1}} \middle| \mathcal{H}_0\right] \\ &= 1 - F_{TW2}\left(\frac{\eta - \mu_{N,M-1}}{\sigma_{N,M-1}}\right), \end{aligned} \tag{32}$$

where $F_{TW2}(\cdot)$ denotes the cumulative distribution function (CDF) of the Tracy-Widom distribution of order 2.

For a given P_{fa}, the threshold is derived as

$$\eta = \mu_{N,M-1} + \sigma_{N,M-1} F_{TW2}^{-1}(1 - P_{\text{fa}}), \tag{33}$$

where $F_{TW2}^{-1}(\cdot)$ denotes the inverse function of $F_{TW2}(\cdot)$.

Fig. 4 illustrates the analytical false alarm probability P_{fa} in (32) with different values of M, N, and η. It shows that an increase in N when $N \gg M$, or an increase in the threshold value of η can result in a notable decrease in the false alarm probability P_{fa}. Conversely, it also reveals that for a fixed threshold, when N is not substantially larger than M, the false alarm probability experiences a notable increase. Furthermore, this figure and (33) provide insights into the selection principle for the threshold η. In practical applications, where a small value of P_{fa} is typically required, the threshold η is determined by the values of M and N. As observed in Fig. 4, increasing M and N under the condition

$N \gg M$ suggests a smaller value of η, while decreasing M and N under the same condition suggests a larger value of η. Additionally, increasing N can significantly reduce the false alarm probability, which implies that the proposed method is more suitable for wide-band RF sources than narrow-band RF sources. This is because wide-band systems inherently support larger values of N, leading to improved detection performance and lower false alarm.

B. MISSED DETECTION PROBABILITY

Under hypothesis $\mathcal{H}_1$, when threshold η is much larger than λ_2/σ_n^2, the reflected RF signal is susceptible to being missed. Thus, we analyze the missed detection probability about the proposed blind detector. In the following parts, we assume that the value of M and N are large enough. Firstly, according to Theorem 1, (18) and (19), the distribution of λ_2 is given in the following lemma.

Lemma 3: When $\Delta\gamma$ is low and $\gamma\|\mathbf{h}_2\|^2 \geq 1$, the distribution of λ_2/σ_n^2 follows

$$\frac{\lambda_2}{\sigma_n^2} \sim \mathcal{N}\left((1+\gamma_1)\left(1+\frac{M-1}{N\gamma_1}\right), \frac{(1+\gamma_1)^2}{N}\right), \tag{34}$$

where $\gamma_1 = \|\mathbf{h}_2\|^2(k-k^2)\gamma$.

Proof: See Appendix-C. ∎

According to Lemma 3, the missed detection probability P_{md} is expressed as

$$\begin{aligned} P_{\text{md}} &= P[Y(\mathbf{Y}) < \eta|\mathcal{H}_1] \\ &= 1 - \mathcal{Q}\left(\frac{\eta - (1+\gamma_1)\left(1+\frac{M-1}{N\gamma_1}\right)}{\frac{1+\gamma_1}{\sqrt{N}}}\right). \end{aligned} \tag{35}$$

It can be concluded from (35) that the missed detection probability is the conditional probability of γ_1, which is time-varying in the same way as $\mathbf{h}_2$. We assume that $f_{\gamma_1}(x)$ is the PDF of γ_1. Hence, we have the following conclusion.

Lemma 4: The average probability of missed detection can be calculated by

$$\begin{aligned} \overline{P_{\text{md}}} &= \int_0^\infty P_{\text{md}}(x) f_{\gamma_1}(x)dx \\ &= 1 - \int_0^\infty \mathcal{Q}\left(\frac{\eta - (1+x)\left(1+\frac{M-1}{Nx}\right)}{\frac{1+x}{\sqrt{N}}}\right) f_{\gamma_1}(x)dx. \end{aligned} \tag{36}$$

C. BIT ERROR RATE

According to (32) and (36), the BER can be written as

$$\begin{aligned} P_e &= \frac{P_{\text{fa}} + \overline{P_{\text{md}}}}{2} \\ &= 1 - \frac{1}{2}\int_0^\infty \mathcal{Q}\left(\frac{\eta - (1+x)\left(1+\frac{M-1}{Nx}\right)}{\frac{1+x}{\sqrt{N}}}\right) f_{\gamma_1}(x)dx \\ &\quad - \frac{1}{2}F_{TW2}\left(\frac{\eta - \mu_{N,M-1}}{\sigma_{N,M-1}}\right). \end{aligned} \tag{37}$$

It is difficult to derive the closed-form expression of the BER. Therefore, we analyze the infimum lower bound of the BER for the blind detector. We assume P_0 and P_1 denote the probability distributions of λ_2/σ_n^2 under the hypotheses of $\mathcal{H}_0$ and $\mathcal{H}_1$, respectively. The total variation [29] can be formulated as

$$\mathcal{V}(P_0\|P_1) \triangleq \frac{1}{2}\|p_0(x) - p_1(x)\|_1, \tag{38}$$

where p_0 and p_1 denote the probability densities of P_0 and P_1, respectively, and $\|\cdot\|_1$ refers to the $\mathcal{L}_1$ norm. According to [30], the BER of the blind detector satisfies

$$P_e \geq 1 - \mathcal{V}(P_0||P_1). \tag{39}$$

where $\mathcal{V}(P_0||P_1)$ is characterized by the following theorem.

Theorem 2: When $\Delta\gamma$ is low, as γ approaches infinity, the total variation between P_0 and P_1 converges to

$$\lim_{\gamma\to\infty} \mathcal{V}(P_0||P_1) \approx \frac{1}{2}\left(1 + \mathcal{Q}\left(-\sqrt{N}\right)\right). \tag{40}$$

Proof: See Appendix-D. ∎

Based on Theorem 2, the lower bound of BER in (39) can be expressed as

$$\lim_{\gamma\to\infty} P_e \geq \frac{1}{2}\left(1 - \mathcal{Q}\left(-\sqrt{N}\right)\right). \tag{41}$$

When $N \to +\infty$, the lower bound of P_e approaches 0. It implies that increasing the value of N can reduce the BER of the proposed blind detector. Furthermore, it is evident that an increase in γ_1 leads to a reduction in the BER. According to Theorem 2, $\gamma_1 = \|\mathbf{h}_2\|^2(k-k^2)\gamma$ depends on the parameters γ and the IDASK. Given a fixed value of γ, the maximum value of γ_1 is achieved when $k = 1/2$. In this case, the proposed blind detector (23) exhibits the optimal detection performance.

V. SIMULATION RESULTS

In this section, we present simulation results to demonstrate the detection performance of the proposed blind detector. Consistent with established AmBC channel models in [25], [26], we set $\gamma \in [0, 70]$ dB to represent diverse ambient RF sources (WiFi/FM), while $\Delta\gamma \in \{-20, -40, -60\}$ dB accounts for dual-path attenuation across practical BD-receiver distances. In the presented simulation results, a Rayleigh fading channel is assumed with the channel path gains $[0, \Delta\gamma]$ dB. We assume the noise variance is $\sigma_n^2 = -20$ dBm, and the value of m in (26) is $m = 3$. Unless otherwise specified, the ambient RF source is assumed to follow a complex Gaussian distribution. The Monte Carlo method is used to calculate the simulated BER, P_{fa}, and P_{md}. For fair comparison, we compare our proposed second largest eigenvalue (SE) based detector with the joint-energy (JE) based blind detector in [15], the largest eigenvalue (LE) based detector in [21], and the improved energy (IE) based detector in [19]. Moreover, we adopt the optimal (OP) detector with perfect CSI and accurate

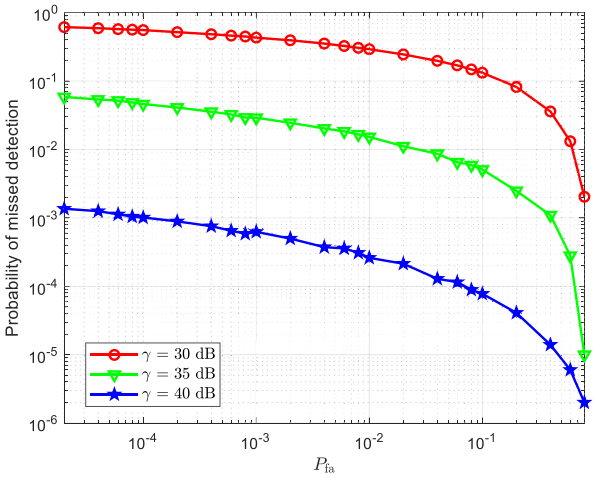

FIGURE 5. Complementary ROC (P_{md} vs. P_{fa}) of the SE detector, where $\gamma = 30, 35, 40$ dB.

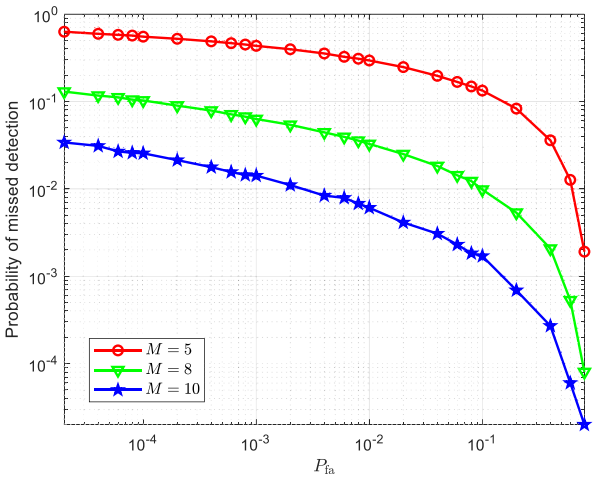

FIGURE 6. Complementary ROC of the SE detector, where $M = 5, 8, 10$.

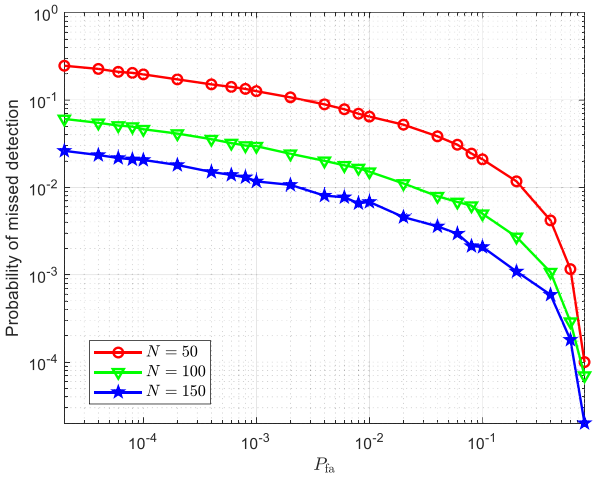

FIGURE 7. Complementary ROC of the SE detector, where $N = 50, 100, 150$.

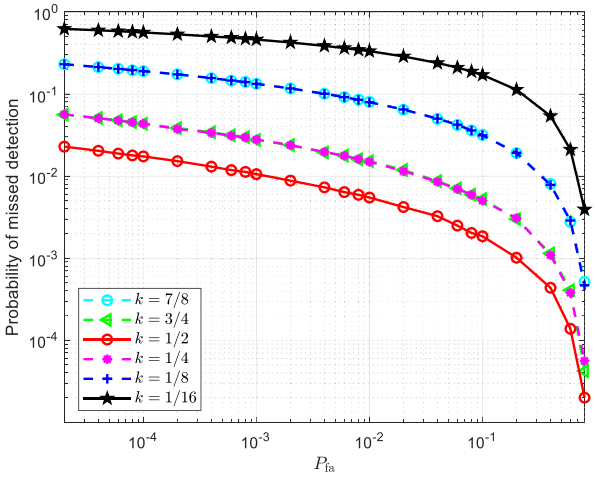

FIGURE 8. Complementary ROC of the SE detector, where $k = 7/8, 3/4, 1/2, 1/4, 1/8, 1/16$.

statistical variances of the received signals and noise as an upper bound benchmark.

Figs. 5 to 8 plot the complementary Receiver Operating characteristics (ROC) curves regarding the probabilities of missed detection versus P_{fa} of the proposed SE detector. Specifically, Fig. 5 shows the probability of missed detection versus P_{fa} under different values of γ. We set $\Delta\gamma = -30$ dB, $M = 5$, and $N = 100$. Indeed, the detection performance of SE detector is noticeably improved as γ increases. Fig. 6 shows the probability of missed detection with different M, where $\gamma = 30$ dB, $\Delta\gamma = -30$ dB, and $N = 100$. It shows that the detection performance of the SE detector is enhanced as M increases, indicating the performance gain provided by spatial diversity. Fig. 7 demonstrates the probability of missed detection with different values of N, where $\gamma = 35$ dB, $\Delta\gamma = -30$ dB and $M = 5$. It shows that the detection performance of the SE detector improves as the N increases. Furthermore, Fig. 8 plots the probability of missed detection of the SE detector with different values of k, where $\gamma = 35$ dB, $\Delta\gamma = -30$ dB, $M = 5$, and $N = 160$. As can be observed in Fig. 8, the SE detector exhibits the optimal detection performance when $k = 1/2$, which is consistent with the analysis in Section IV-C.

Figs. 9 to 11 plot the simulated BER versus γ of the JE, LE, SE, IE and OP detectors with different values of $\Delta\gamma$. The number of antennas at the receiver is set as $M = 5$ and the BD symbol period is $N = 100$. In the JE and LE detectors, accurate statistical variances of the received signals are used for the calculation of the detection threshold. In the IE detector, the perfect CSI estimation is assumed. The BER of OP detector is provided as an upper bound benchmark. In the SE detector, the detection threshold η is calculated by $P_{\text{fa}} = 10^{-3}$. It can be observed that for large values of γ, the BERs of the SE detector are significantly lower than those of the JE, LE, and IE detectors. For different values of $\Delta\gamma$, the proposed SE detector exhibits a higher BER compared to JE, LE, and IE detectors at low values of γ. Conversely, as γ increases, the proposed SE detector

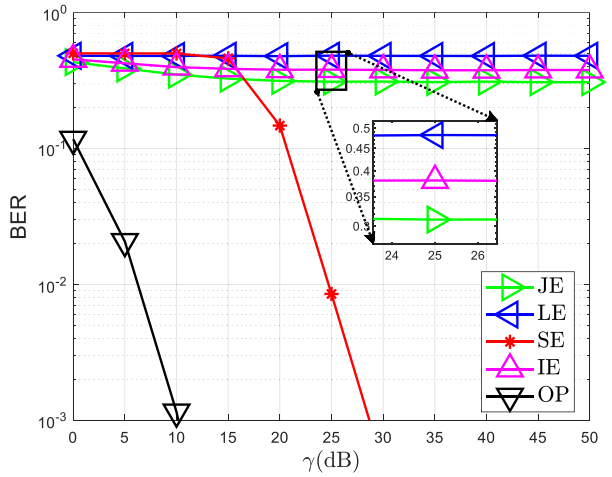

FIGURE 9. Simulated BER versus γ for the JE, LE, SE, IE and OP detectors, where $\Delta\gamma = -20$ dB.

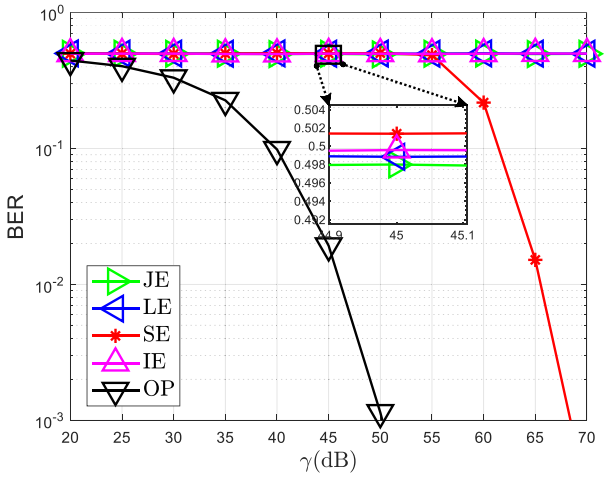

FIGURE 11. Simulated BER versus γ for the JE, LE, SE, IE and OP detectors, where $\Delta\gamma = -60$ dB.

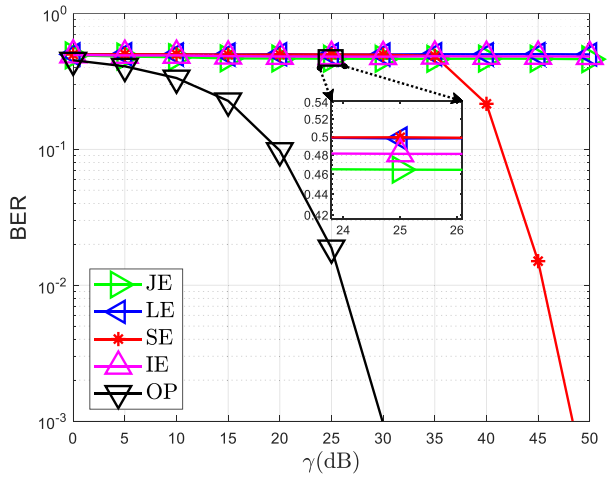

FIGURE 10. Simulated BER versus γ for the JE, LE, SE, IE and OP detectors, where $\Delta\gamma = -40$ dB.

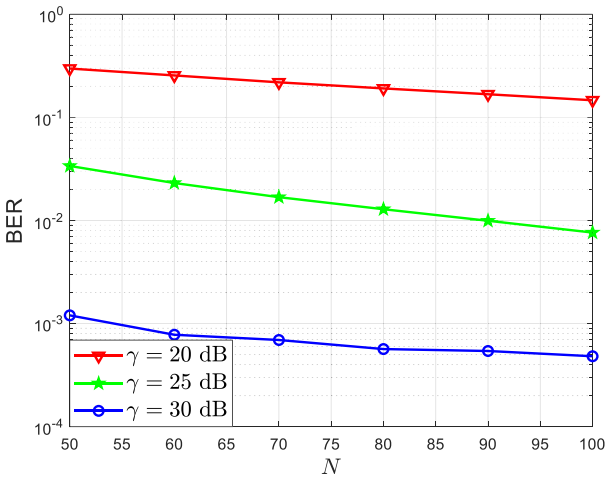

FIGURE 12. Simulated BER versus N of the SE detector with different values of γ.

achieves a significant improvement in BER performance, outperforming the other detectors. This demonstrates the robustness and effectiveness of the proposed SE detector in high SNR regimes. However, for large values of $\Delta\gamma$, such as $\Delta\gamma = -60$ dB, a substantially high SNR is required. To relax this high SNR requirement, we will investigate potential solutions in our future research.

Fig. 12 plots the simulated BER versus N of the SE detector with different values of γ. We set $M = 5$, $\Delta\gamma = -20$ dB and $P_{\text{fa}} = 10^{-2}$. It can be observed that the BER of the SE detector decreases with the increases of N. Fig. 13 plots the simulated BER versus k of the SE detector with different values of γ. We set $M = 5$, $N = 100$, $\Delta\gamma = -20$ dB and $P_{\text{fa}} = 10^{-2}$. It shows that the proposed method achieves the lowest BER when $k = 1/2$, which is consistent with the theoretical analysis in Section III. Fig. 14 compares the simulated BER versus γ of the SE and OP detectors with varying digital modulation types in the ambient RF signal. The digital modulation types are BPSK, QPSK, and 16-QAM. This figure demonstrates that the proposed SE detector exhibits a similar BER performance for different digital modulation types.

Fig. 15 plots the simulated BER of the SE detector with the number of receive antennas $M = 3, 4, 5, 6, 7, 8, 9, 10$. We set $N = 100$, $\Delta\gamma = -20$ dB, and $P_{\text{fa}} = 10^{-3}$. It can be seen that for all values of M, the proposed detector achieves a notable improvement in BER performance as γ increases. For example, when $M = 3$, as γ increases from 20 dB to 30 dB, the BER decreases from 0.45 to 0.06.

In Fig. 16, we introduce a metric σ_{n1}^2, referred to as the average power of interference from other sources, to quantify the impact of additional interference on the BER performance of the proposed detector. The simulation parameters are set as $M = 5$, $N = 100$, $\Delta\gamma = -20$ dB, $\gamma = 30$ dB, and $P_{\text{fa}} = 10^{-3}$. The channels between the interference sources and the receiver are modeled as Rayleigh fading channels, and the signals from the interference sources are assumed to follow complex Gaussian distributions. As

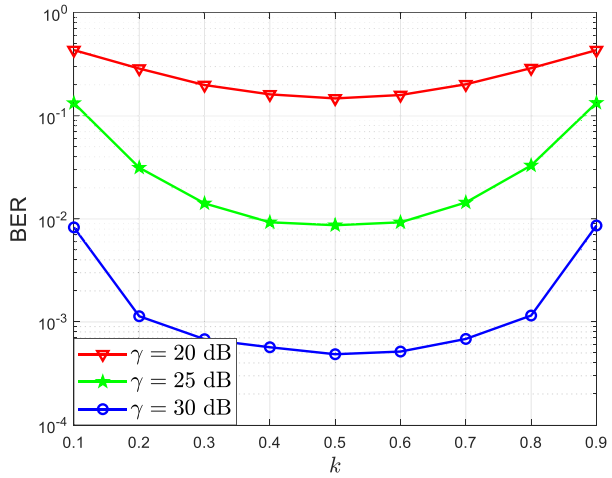

FIGURE 13. Simulated BER versus k of the SE detector with different values of γ.

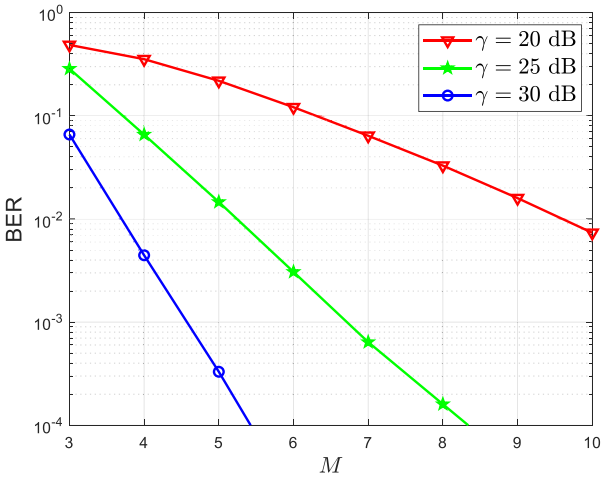

FIGURE 15. Simulated BER versus M of the SE detector with different values of γ.

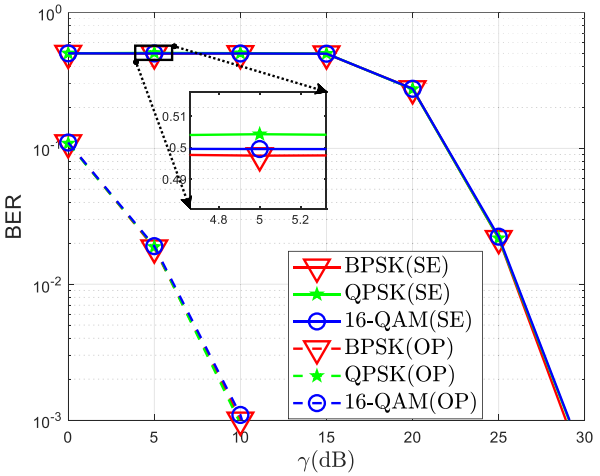

FIGURE 14. Simulated BER versus γ of the SE and OP detectors. The ambient RF signal employs a variety of digital modulation types, including BPSK, QPSK, and 16-QAM.

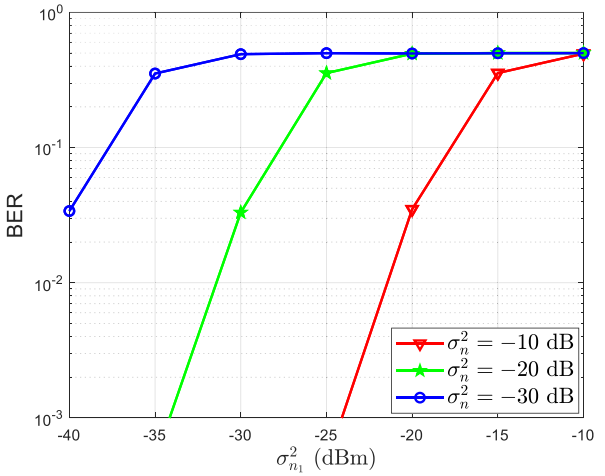

FIGURE 16. Simulated BER versus the average power of interference from other RF sources for the SE detector with different values of σ_n^2.

observed in the results, the BER performance of the proposed detector degrades significantly as the interference power from other sources increases.

Furthermore, we investigate the impact of sampling frequency offset on the proposed method. To quantify this impact, we define a parameter called the sampling offset N_{offset}, which measures the number of sampling points by which the actual sampling instants deviate from the optimal sampling points. Specifically, $N_{\text{offset}} < 0$, $N_{\text{offset}} = 0$, and $N_{\text{offset}} > 0$ correspond to the advanced, optimal, and delayed sampling, respectively. As can be observed in Fig. 17, when $N_{\text{offset}} > 0$, a moderate sampling offset has a small effect on the BER performance of the proposed detector. In contrast, when $N_{\text{offset}} < 0$, a moderate sampling offset causes a significant degradation in BER performance.

Fig. 18 shows the simulated and analytical BER versus M of SE detector for a large value of γ, where $P_{\text{fa}} = 10^{-1}, 10^{-2}, 10^{-3}$. The noise variance is estimated using the unmodified scheme in (25) and the modified scheme in (26). We set $\gamma = 30$ dB, $\Delta\gamma = -20$ dB, and $N = 20M$. As the values of M and N increase, all the BER curves converge to the analytical curves of $P_{\text{fa}}/2$. More importantly, the BER performance of the modified noise estimation scheme outperforms that of the unmodified scheme.

Fig. 19 plots the simulated and analytical probability of missed detection versus γ of the SE detector with different values of $\Delta\gamma$. We set $M = 10$, $N = 100$, and $P_{\text{fa}} = 10^{-2}$. It can be seen that the theoretical curves align closely with the simulation results, validating the accuracy of the derived expressions of (35) and (36). Fig. 20 plots the simulated and analytical probability of false alarm versus M of the SE detector with different values of P_{fa}. We set $N = 20M$, $\Delta\gamma = -20$ dB, and $\gamma = 30$ dB. It can be seen that as M and N increase, the simulated probabilities of false alarm approach to the theoretical curves in (32).

To investigate the impact of the number of antennas M to the false alarm probability P_{fa}, Fig. 20 plots simulated and analytical probability of false alarm versus M for

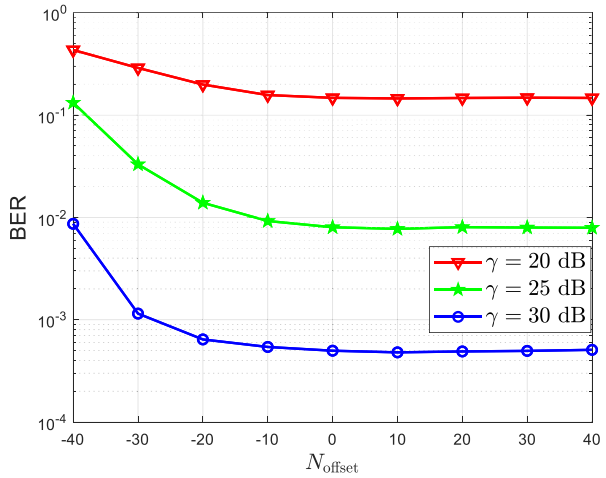

FIGURE 17. Simulated BER versus N_{offset} of the proposed SE detector with varying values of γ.

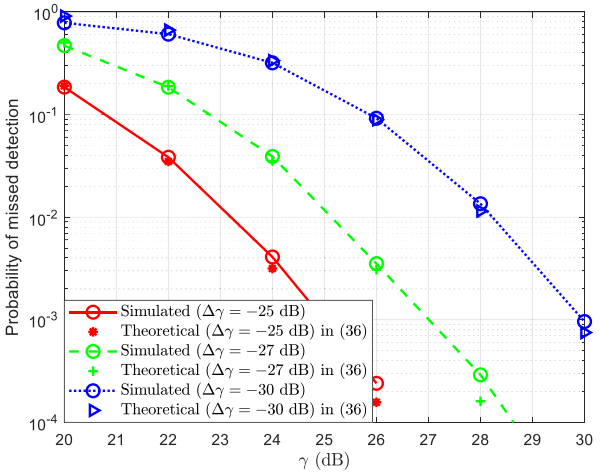

FIGURE 19. Simulated and analytical probability of missed detection versus γ of the SE detector with different values of $\Delta\gamma$.

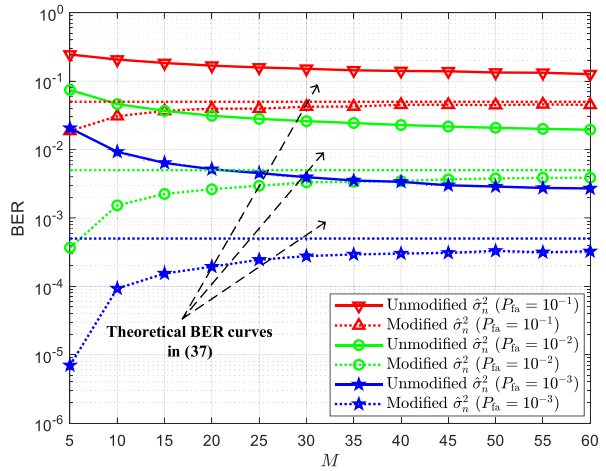

FIGURE 18. Simulated and analytical BER versus M for the SE detector under different P_{fa} and different estimation schemes of $\hat{\sigma}_n^2$.

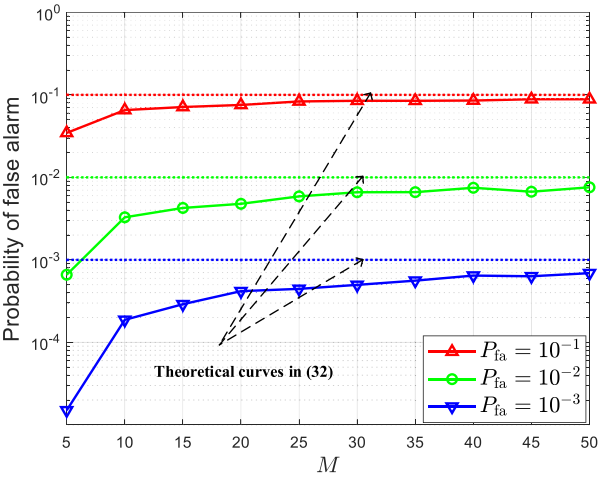

FIGURE 20. Simulated and analytical probability of false alarm versus M of the SE detector with different values of P_{fa}.

the SE detector under different values of P_{fa}. We set $N = 20M$, $\Delta\gamma = -20$ dB, and $\gamma = 30$ dB. For each $M \in \{5, 10, 15, \ldots, 50\}$, the corresponding threshold is recalculated by (33) to maintain the targeted $P_{\text{fa}} \in \{10^{-1}, 10^{-2}, 10^{-3}\}$. The results demonstrate two key observations: 1) a large discrepancy exists between theoretical and simulated results for small values of M; 2) the simulated P_{fa} approach to the theoretical curves derived from (32) as M increases.

Fig. 21 illustrates the throughput versus the received SNR γ of the non-coherent detector in [21], coherent detector in [12], and the proposed detector. We assume that all three detectors operate under identical conditions in terms of band-width, packet error rate and protocol efficiency. For the coherent detector and the proposed detector, the same bandwidth is allocated for data transmission. The non-coherent detector utilizes 40% of the bandwidth for data transmission, with the remaining 60% reserved for pilot signals. As can be observed from Fig. 21, the proposed detector possesses the same throughput as the coherent detector and the higher throughput than the non-coherent detector.

Fig. 22 plots the simulated BER versus γ of the proposed SE detector for relatively small values of $\Delta\gamma$. We set $M = 5$, $N = 100$, and $P_{\text{fa}} = 10^{-3}$. This figure shows that the proposed detector achieves a significantly improved BER performance as $\Delta\gamma$ increases.

VI. CONCLUSION

A. SUMMARY OF CONTRIBUTIONS

This paper investigated the blind symbol detection problem of the AmBC system. Firstly, by leveraging IDASK, the second largest eigenvalue of the received signal covariance matrix was distinguished from the DLI in the proposed blind symbol detector. Moreover, an improved noise estimation scheme was presented to enhance the accuracy of noise variance estimation. Secondly, a theoretical analysis was conducted to evaluate the false alarm probability and the

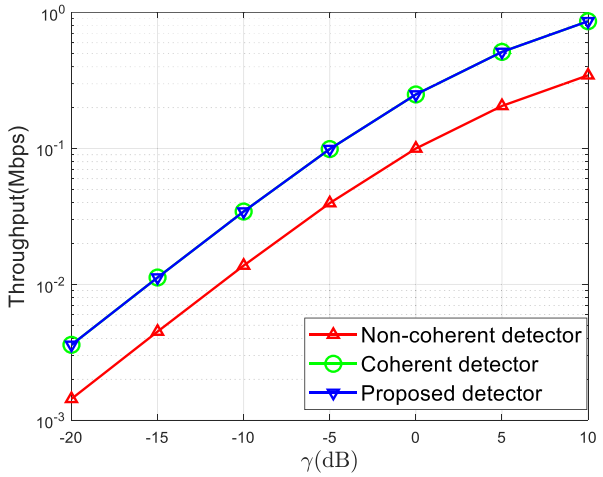

FIGURE 21. Throughput versus the received SNR γ of the non-coherent detector, coherent detector, and proposed detector.

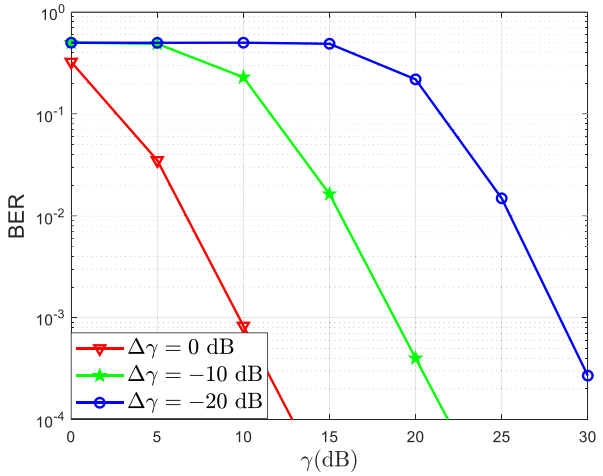

FIGURE 22. Simulated BER versus γ of the proposed SE detector for relatively small values of $\Delta\gamma$.

missed detection probability of the blind detector, followed by a lower BER bound. Finally, the simulation results validated that the proposed detector exhibits the optimal detection performance with IDASK using a reflection ratio of 50%, i.e., $k = 1/2$, and exhibits a great detection performance compared to conventional counterparts.

B. CHALLENGES AND FUTURE WORK

- In real-world scenarios, ambient RF environment may be highly dynamic, and the ambient RF signals do not follow a Gaussian distribution, posing significant challenges for our proposed method in achieving optimal detection performance. Furthermore, in multi-user environments, the increased interference from multiple RF sources complicates the IDASK-aided modulation in the AmBC systems, potentially degrading system efficiency and reliability. Addressing these challenges will be the focus of our future work.
- A significant challenge for the proposed method is to achieve high data rate transmission due to the binary IDASK-aided modulation. While the current framework is optimized for binary modulation, future work will investigate the potential extension to higher-order modulation schemes in AmBC systems.
- Due to the sensitivity of the proposed detector to external interference, it is essential to develop strategies for mitigating multi-source interference in future research to enhance the robustness of AmBC systems.

APPENDIX

A. PROOF OF THEOREM 1

Under hypothesis $\mathcal{H}_1$, the following matrix is first constructed

$$\bar{\mathbf{R}}_1 = \begin{bmatrix} 1 & 0 & (\mathbf{h}_1+\mathbf{h}_2)^H \\ 0 & 1 & \mathbf{h}_1^H \\ \mathbf{0}_{M\times 1} & \mathbf{0}_{M\times 1} & \mathbf{R}_1 \end{bmatrix}. \tag{43}$$

It is inferred from (14) and (43) that $\det(\bar{\mathbf{R}}_1) = \det(\mathbf{R}_1)$. Then, multiplying the following lower triangular matrix

$$\mathbf{A} = \begin{bmatrix} 1 & 0 & \mathbf{0}_{1\times M} \\ 0 & 1 & \mathbf{0}_{1\times M} \\ -k\sigma_s^2(\mathbf{h}_1+\mathbf{h}_2) & -(1-k)\sigma_s^2\mathbf{h}_1 & \mathbf{I}_M \end{bmatrix} \tag{44}$$

by $\bar{\mathbf{R}}_1$, namely, $\mathbf{A}\bar{\mathbf{R}}_1$, yields

$$\begin{bmatrix} 1 & 0 & (\mathbf{h}_1+\mathbf{h}_2)^H \\ 0 & 1 & \mathbf{h}_1^H \\ -k\sigma_s^2(\mathbf{h}_1+\mathbf{h}_2) & -(1-k)\sigma_s^2\mathbf{h}_1 & \sigma_n^2\mathbf{I}_M \end{bmatrix}. \tag{45}$$

Moreover, based on the product of the following upper triangular matrix

$$\mathbf{B} = \begin{bmatrix} 1 & 0 & -\frac{(\mathbf{h}_1+\mathbf{h}_2)^H}{\sigma_n^2} \\ 0 & 1 & -\frac{\mathbf{h}_1^H}{\sigma_n^2} \\ \mathbf{0}_{M\times 1} & \mathbf{0}_{M\times 1} & \mathbf{I}_M \end{bmatrix} \tag{46}$$

and the matrix in (45), $\bar{\mathbf{R}}_1$ can be transformed as

$$\begin{bmatrix} \frac{k\sigma_s^2\|(\mathbf{h}_1+\mathbf{h}_2)\|^2}{\sigma_n^2}+1 & \frac{(1-k)\sigma_s^2(\mathbf{h}_1+\mathbf{h}_2)^H\mathbf{h}_1}{\sigma_n^2} & \mathbf{0}_{1\times M} \\ \frac{k\sigma_s^2\mathbf{h}_1^H(\mathbf{h}_1+\mathbf{h}_2)}{\sigma_n^2} & \frac{(1-k)\sigma_s^2\|\mathbf{h}_1\|^2}{\sigma_n^2}+1 & \mathbf{0}_{1\times M} \\ -k\sigma_s^2(\mathbf{h}_1+\mathbf{h}_2) & -(1-k)\sigma_s^2\mathbf{h}_1 & \sigma_n^2\mathbf{I}_M \end{bmatrix}. \tag{47}$$

$$\det(\mathbf{R}_1) = \underbrace{\left(\sigma_s^2\|\mathbf{h}_1\|^2+\sigma_n^2\right)\left(\left(k-k^2\right)\sigma_s^2\|\mathbf{h}_2\|^2+\sigma_n^2\right)\left(\sigma_n^2\right)^{M-2}}_{\text{P1}}$$
$$+\underbrace{(k)^2\sigma_s^2\sigma_n^M\|\mathbf{h}_2\|^2+k\sigma_s^2\sigma_n^M\left(\mathbf{h}_1^H\mathbf{h}_2+\mathbf{h}_2^H\mathbf{h}_1\right)-\left(k-k^2\right)\sigma_s^4\left\|\mathbf{h}_2^H\mathbf{h}_1\right\|^2\left(\sigma_n^2\right)^{M-2}}_{\text{P2}}. \tag{42}$$

Based on the transformations of $\mathbf{R}_1$ from (43) to (47), the determinant of $\mathbf{R}_1$ is obtained in (42), shown at bottom of the page. As $\Delta\gamma \to 0$ and $\mathbf{h}_1$ and $\mathbf{h}_2$ are independent of each other, the value of P2 in (42) is significantly smaller than that of P1. Consequently, Theorem 1 is proved.

B. PROOF OF LEMMA 1

We first formulate a binary hypothesis testing when the receiver is equipped with $M-1$ antennas. In the presence of a direct channel, the null hypothesis $\mathcal{H}_0$ is applicable. Conversely, in the absence of a direct channel, the alternative hypothesis $\mathcal{H}_1$ is relevant. Thus, the received signal $\bar{\mathbf{Y}} = [\mathbf{y}_1, \mathbf{y}_2, \ldots, \mathbf{y}_N] \in \mathbf{C}^{(M-1)\times N}$ follows

$$\bar{\mathbf{Y}} \sim \begin{cases} \mathcal{CN}\left(0, \bar{\mathbf{R}}_0\right), & \mathcal{H}_0, \\ \mathcal{CN}\left(0, \bar{\mathbf{R}}_1\right), & \mathcal{H}_1, \end{cases} \tag{48}$$

where $\bar{\mathbf{R}}_0 = \sigma_s^2 \bar{\mathbf{h}}_1 \bar{\mathbf{h}}_1^H + \sigma_n^2 \mathbf{I}_{M-1}$, $\bar{\mathbf{R}}_1 = \sigma_n^2 \mathbf{I}_{M-1}$, and $\bar{\mathbf{h}}_1$ denotes the direct channel vector. We assume that the covariance matrix of $\bar{\mathbf{Y}}$ is $\bar{\mathbf{R}}$, whose eigenvalues satisfy $\bar{\lambda}_1 \geq \bar{\lambda}_2 \geq \cdots \geq \bar{\lambda}_{M-1}$. Under hypothesis $\mathcal{H}_0$, according to [31], [32], the distribution of the largest eigenvalue of $\bar{\mathbf{R}}$ follows

$$\bar{\lambda}_1^0/\sigma_n^2 \sim \mathcal{N}\left((1+\gamma_0)\left(1+\frac{M-2}{N\gamma_0}\right), \frac{(1+\gamma_0)^2}{N}\right), \tag{49}$$

where $\bar{\lambda}_m^i$ is the m-th eigenvalue of $\bar{\mathbf{R}}$ under hypothesis $\mathcal{H}_i$ for $m = 1, 2, \ldots, M-1$ and $i = \{0, 1\}$, and $\gamma_0 = \|\bar{\mathbf{h}}_1\|^2 \gamma$. Then, under hypothesis $\mathcal{H}_1$, based on [33], the distribution of the largest eigenvalue of $\bar{\mathbf{R}}$ satisfies

$$\frac{\bar{\lambda}_1^1/\sigma_n^2 - \mu_{N,M-1}}{\sigma_{N,M-1}} \sim TW_2. \tag{50}$$

In the original hypotheses of (7), for hypothesis $\mathcal{H}_0$, λ_1 and λ_2 of $\hat{\mathbf{R}}$ in (17) can be recalculated as

$$\lambda_1/\sigma_n^2 = \max\{\bar{\lambda}_1^0/\sigma_n^2, \bar{\lambda}_1^1/\sigma_n^2\}, \tag{51}$$

$$\lambda_2/\sigma_n^2 = \min\{\bar{\lambda}_1^0/\sigma_n^2, \bar{\lambda}_1^1/\sigma_n^2\}. \tag{52}$$

The PDFs of $\bar{\lambda}_1^0/\sigma_n^2$ and $\bar{\lambda}_1^1/\sigma_n^2$ is denoted by $\bar{p}_0$ and $\bar{p}_1$, respectively. According to the definition of the overlapping coefficient (OVL) in [34], for any $a \in (-\infty, +\infty)$, the OVL of $\bar{\lambda}_1^0/\sigma_n^2$ and $\bar{\lambda}_1^1/\sigma_n^2$ is written as

$$\begin{aligned} \text{OVL} &= \int_{-\infty}^{+\infty} \min\{\bar{p}_0(x), \bar{p}_1(x)\}dx \\ &= \int_{a}^{+\infty} \min\{\bar{p}_0(x), \bar{p}_1(x)\}dx + \int_{-\infty}^{a} \min\{\bar{p}_0(x), \bar{p}_1(x)\}dx \\ &\leq \int_{a}^{\infty} \bar{p}_1(x)dx + \int_{-\infty}^{a} \bar{p}_0(x)dx. \end{aligned} \tag{53}$$

Based on (49), we have

$$\int_{-\infty}^{a} \bar{p}_0(x)dx = 1 - \mathcal{Q}\left(\frac{a - (1+\gamma_0)\left(1+\frac{M-2}{N\gamma_0}\right)}{\frac{(1+\gamma_0)}{\sqrt{N}}}\right). \tag{54}$$

As $\gamma \to +\infty$, (54) can be approximated as

$$\int_{-\infty}^{a} \bar{p}_0(x)dx \approx 1 - \mathcal{Q}\left(-\sqrt{N}\right) \approx 0. \tag{55}$$

Furthermore, based on (50), through numerical calculation, we obtain $\int_0^5 \bar{p}_1(x)dx = 1 - 10^{-10}$. Consequently, for a large value of a, such as $a > 5$, we have $\int_a^{+\infty} \bar{p}_1(x)dx \approx 0$.

Therefore, for $\gamma \to +\infty$ and a large value of a, the OVL in (53) approaches zero. In this case, the distribution of λ_2/σ_n^2 can be approximated by the distribution of $\bar{\lambda}_1^1/\sigma_n^2$. Thus, Lemma 1 is proved.

C. PROOF OF LEMMA 3

Similar to Appendix-B, we also formulate a binary hypothesis testing when the receiver is equipped with $M-1$ antennas. In the presence of the direct channel, the null hypothesis $\mathcal{H}_0$ is applicable. In the presence of the cascaded channel, the alternative hypothesis $\mathcal{H}_1$ is relevant. Thus, the received signal $\bar{\mathbf{Y}} = [\mathbf{y}_1, \mathbf{y}_2, \ldots, \mathbf{y}_N] \in \mathbf{C}^{(M-1)\times N}$ follows

$$\bar{\mathbf{Y}} \sim \begin{cases} \mathcal{CN}\left(0, \bar{\mathbf{R}}_0\right), & \mathcal{H}_0, \\ \mathcal{CN}\left(0, \bar{\mathbf{R}}_1\right), & \mathcal{H}_1, \end{cases} \tag{56}$$

where $\bar{\mathbf{R}}_0 = \sigma_s^2 \bar{\mathbf{h}}_1 \bar{\mathbf{h}}_1^H + \sigma_n^2 \mathbf{I}_{M-1}$, $\bar{\mathbf{R}}_1 = \sigma_s^2 \bar{\mathbf{h}}_2 \bar{\mathbf{h}}_2^H K + \sigma_n^2 \mathbf{I}_{M-1}$, $\bar{\mathbf{h}}_1$ and $\bar{\mathbf{h}}_2$ denote the direct and cascaded channels, respectively, and $K = k - k^2$. Under hypothesis $\mathcal{H}_i (i \in \{0, 1\})$, the distribution of the largest eigenvalue $\bar{\lambda}_1^i/\sigma_n^2$ of $\bar{\mathbf{R}}$ satisfies [31]

$$\bar{\lambda}_1^i/\sigma_n^2 \sim \mathcal{N}\left((1+\gamma_i)\left(1+\frac{M-2}{N\gamma_i}\right), \frac{(1+\gamma_i)^2}{N}\right). \tag{57}$$

where $\gamma_0 = \|\bar{\mathbf{h}}_1\|^2 \gamma$ and $\gamma_1 = \|\bar{\mathbf{h}}_2\|^2 K\gamma$.

According to [21], the OVL of $\bar{\lambda}_1^0/\sigma_n^2$ and $\bar{\lambda}_1^1/\sigma_n^2$ can be expressed as

$$\text{OVL} = \mathcal{Q}\left(\frac{\sqrt{N}\gamma - \frac{M-2}{\sqrt{N}\gamma\|\bar{\mathbf{h}}_1\|^2\|\bar{\mathbf{h}}_2\|^2}}{\left(\|\bar{\mathbf{h}}_1\|^2 + K\|\bar{\mathbf{h}}_2\|^2\right)\gamma + 2}\left(\left|\|\bar{\mathbf{h}}_1\|^2 - K\|\bar{\mathbf{h}}_2\|^2\right|\right)\right). \tag{58}$$

When $\Delta\gamma \to 0$ and $\gamma\|\bar{\mathbf{h}}_2\|^2 \geq 1$, (58) is approximated as

$$\begin{aligned} \text{OVL} &= \mathcal{Q}\left(\frac{\sqrt{N}\gamma - \frac{M-2}{\sqrt{N}\gamma\|\bar{\mathbf{h}}_1\|^2\|\bar{\mathbf{h}}_2\|^2}}{\left(1 + K\frac{\|\bar{\mathbf{h}}_2\|^2}{\|\bar{\mathbf{h}}_1\|^2}\right)\gamma + \frac{2}{\|\bar{\mathbf{h}}_1\|^2}}\left(\left|1 - K\frac{\|\bar{\mathbf{h}}_2\|^2}{\|\bar{\mathbf{h}}_1\|^2}\right|\right)\right) \\ &\approx \mathcal{Q}\left(\frac{\sqrt{N}\gamma - \frac{M-2}{\sqrt{N}\gamma\|\bar{\mathbf{h}}_1\|^2\|\bar{\mathbf{h}}_2\|^2}}{\gamma + \frac{2}{\|\bar{\mathbf{h}}_1\|^2}}\right) \\ &\approx \mathcal{Q}\left(\frac{\sqrt{N}\gamma}{\gamma + \frac{2}{\|\bar{\mathbf{h}}_1\|^2}}\right). \end{aligned} \tag{59}$$

Eq. (59) shows that for a large value of N, the OVL approaches 0. Therefore, based on (51) and (52), the

distribution of the second largest eigenvalue λ_2/σ_n^2 can be approximated by the distribution of $\bar{\lambda}_1^1/\sigma_n^2$. Lemma 3 is proved.

D. PROOF OF THEOREM 2

The total variation between P_0 and P_1 is written as

$$\begin{aligned}\lim_{\gamma\to\infty}\mathcal{V}(P_0\|P_1) &= \lim_{\gamma\to\infty}\frac{1}{2}\int_0^{\infty}|p_0(x)-p_1(x)|dx\\ &= \frac{1}{2}\int_0^{a}\left|p_0(x)-\lim_{\gamma\to\infty}p_1(x)\right|dx\\ &\quad+\frac{1}{2}\int_a^{\infty}\left|p_0(x)-\lim_{\gamma\to\infty}p_1(x)\right|dx, \quad (60)\end{aligned}$$

where a is a non-negative large number. Through numerical calculations, for a large value of a, we have $\int_a^{\infty}p_0(x)dx\approx 0$. In this case, the probability of $p_1(x)$ in the interval $[a,+\infty]$ is expressed as

$$\begin{aligned}\lim_{\gamma\to\infty}\int_a^{\infty}p_1(x)dx &= \lim_{\gamma\to\infty}\mathcal{Q}\left(\frac{a-(1+\gamma_1)\left(1+\frac{M-1}{N\gamma_1}\right)}{\frac{(1+\gamma_1)}{\sqrt{N}}}\right)\\ &= \mathcal{Q}\left(-\sqrt{N}\right), \quad (61)\end{aligned}$$

where $\gamma_1=\|\mathbf{h}_2\|^2(k-k^2)\gamma$. Consequently, we have

$$\begin{aligned}\lim_{\gamma\to\infty}\mathcal{V}(P_0\|P_1) &\approx \frac{1}{2}\int_0^{a}p_0(x)dx+\lim_{\gamma\to\infty}\frac{1}{2}\int_a^{\infty}p_1(x)dx\\ &\approx \frac{1}{2}\left(1+\mathcal{Q}\left(-\sqrt{N}\right)\right). \quad (62)\end{aligned}$$

Theorem 2 is proved.

REFERENCES

[1] T. Islam, S. C. Mukhopadhyay, and N. K. Suryadevara, "Smart sensors and Internet of Things: A postgraduate paper," *IEEE Sensors J.*, vol. 17, no. 3, pp. 577–584, Feb. 2017.

[2] T. Jiang et al., "Backscatter communication meets practical battery-free Internet of Things: A survey and outlook," *IEEE Commun. Surveys Tuts.*, vol. 25, no. 3, pp. 2021–2051, 3rd Quart., 2023.

[3] N. Van Huynh, D. T. Hoang, X. Lu, D. Niyato, P. Wang, and D. I. Kim, "Ambient backscatter communications: A contemporary survey," *IEEE Commun. Surveys Tuts.*, vol. 20, no. 4, pp. 2889–2922, 4th Quart., 2018.

[4] D. T. Hoang, D. Niyato, P. Wang, D. I. Kim, and Z. Han, "Ambient backscatter: A new approach to improve network performance for RF-powered cognitive radio networks," *IEEE Trans. Commun.*, vol. 65, no. 9, pp. 3659–3674, Sep. 2017.

[5] R. Long, Y.-C. Liang, H. Guo, G. Yang, and R. Zhang, "Symbiotic radio: A new communication paradigm for passive Internet of Things," *IEEE Internet Things J.*, vol. 7, no. 2, pp. 1350–1363, Feb. 2020.

[6] G. Yang, Y.-C. Liang, R. Zhang, and Y. Pei, "Modulation in the air: Backscatter communication over ambient OFDM carrier," *IEEE Trans. Commun.*, vol. 66, no. 3, pp. 1219–1233, Mar. 2018.

[7] D. Darsena, G. Gelli, and F. Verde, "Modeling and performance analysis of wireless networks with ambient backscatter devices," *IEEE Trans. Commun.*, vol. 65, no. 4, pp. 1797–1814, Apr. 2017.

[8] G. Yang, Q. Zhang, and Y.-C. Liang, "Cooperative ambient backscatter communications for green Internet-of-Things," *IEEE Internet Things J.*, vol. 5, no. 2, pp. 1116–1130, Apr. 2018.

[9] Q. Zhang, H. Guo, Y.-C. Liang, and X. Yuan, "Constellation learning-based signal detection for ambient backscatter communication systems," *IEEE J. Sel. Areas Commun.*, vol. 37, no. 2, pp. 452–463, Feb. 2019.

[10] H. Chen, Y.-Y. Wei, H. Chen, and W.-Q. Wang, "Adaptive detection for multi-antenna ambient backscatter communications system with MFSK modulation," *IEEE Internet Things J.*, vol. 11, no. 16, pp. 26819–26825, Aug. 2024.

[11] Y.-Q. Hu, H. Chen, S.-L. Ji, W.-Q. Wang, and H. Chen, "Adaptive detector for FDA-based ambient backscatter communications," *IEEE Trans. Wireless Commun.*, vol. 21, no. 12, pp. 10381–10392, Dec. 2022.

[12] Q. Tao, C. Zhong, X. Chen, H. Lin, and Z. Zhang, "Optimal detection for ambient backscatter communication systems with multiantenna reader under complex gaussian illuminator," *IEEE Internet Things J.*, vol. 7, no. 12, pp. 11371–11383, Dec. 2020.

[13] G. Wang, F. Gao, R. Fan, and C. Tellambura, "Ambient backscatter communication systems: Detection and performance analysis," *IEEE Trans. Commun.*, vol. 64, no. 11, pp. 4836–4846, Nov. 2016.

[14] Q. Tao, C. Zhong, H. Lin, and Z. Zhang, "Symbol detection of ambient backscatter systems with manchester coding," *IEEE Trans. Wireless Commun.*, vol. 17, no. 6, pp. 4028–4038, Jun. 2018.

[15] J. Qian, F. Gao, G. Wang, S. Jin, and H. Zhu, "Noncoherent detections for ambient backscatter system," *IEEE Trans. Wireless Commun.*, vol. 16, no. 3, pp. 1412–1422, Mar. 2017.

[16] G. Yang, Z. Luo, N. Jin, Y.-C. Liang, Y. Xu, and G. Wang, "Non-coherent parallel detection of ambient backscatter communications with multiple tags," *IEEE Trans. Veh. Technol.*, vol. 72, no. 4, pp. 5344–5349, Apr. 2023.

[17] C. Chen, G. Wang, H. Guan, Y.-C. Liang, and C. Tellambura, "Transceiver design and signal detection in backscatter communication systems with multiple-antenna tags," *IEEE Trans. Wireless Commun.*, vol. 19, no. 5, pp. 3273–3288, May 2020.

[18] S. Ma, G. Wang, R. Fan, and C. Tellambura, "Blind channel estimation for ambient backscatter communication systems," *IEEE Commun. Lett.*, vol. 22, no. 6, pp. 1296–1299, Jun. 2018.

[19] Y. Chen and W. Feng, "Novel signal detectors for ambient backscatter communications in Internet of Things applications," *IEEE Internet Things J.*, vol. 11, no. 3, pp. 5388–5400, Feb. 2024.

[20] S. Guruacharya, X. Lu, and E. Hossain, "Optimal non-coherent detector for ambient backscatter communication system," *IEEE Trans. Veh. Technol.*, vol. 69, no. 12, pp. 16197–16201, Dec. 2020.

[21] Q. Tao, C. Zhong, X. Chen, H. Lin, and Z. Zhang, "Maximum-eigenvalue detector for multiple antenna ambient backscatter communication systems," *IEEE Trans. Veh. Technol.*, vol. 68, no. 12, pp. 12411–12415, Dec. 2019.

[22] J. Qian, F. Gao, G. Wang, S. Jin, and H. Zhu, "Semi-coherent detection and performance analysis for ambient backscatter system," *IEEE Trans. Commun.*, vol. 65, no. 12, pp. 5266–5279, Dec. 2017.

[23] W. Liu, S. Shen, D. H. K. Tsang, R. K. Mallik, and R. Murch, "An efficient ratio detector for ambient backscatter communication," *IEEE Trans. Wireless Commun.*, vol. 23, no. 6, pp. 5908–5921, Jun. 2024.

[24] W. Zhao, G. Wang, S. Atapattu, and B. Ai, "Blind channel estimation in ambient backscatter communication systems with multiple-antenna reader," in *Proc. IEEE/CIC Int. Conf. Commun. China (ICCC)*, Aug. 2018, pp. 320–324.

[25] H. Guo, Q. Zhang, S. Xiao, and Y.-C. Liang, "Exploiting multiple antennas for cognitive ambient backscatter communication," *IEEE Internet Things J.*, vol. 6, no. 1, pp. 765–775, Feb. 2019.

[26] S. Zargari, A. Hakimi, F. Rezaei, C. Tellambura, and A. Maaref, "Signal detection in ambient backscatter systems: Fundamentals, methods, and trends," *IEEE Access*, vol. 11, pp. 140287–140324, 2023.

[27] A. Taherpour, M. Nasiri-Kenari, and S. Gazor, "Multiple antenna spectrum sensing in cognitive radios," *IEEE Trans. Wireless Commun.*, vol. 9, no. 2, pp. 814–823, Feb. 2010.

[28] V. A. Marvcenko and L. A. Pastur, "Distribution of eigenvalues for some sets of random matrices," *Math. USSR-Sbornik*, vol. 1, pp. 457–483, Apr. 1967.

[29] B. A. Bash, D. Goeckel, and D. Towsley, "Limits of reliable communication with low probability of detection on AWGN channels," *IEEE J. Sel. Areas Commun.*, vol. 31, no. 9, pp. 1921–1930, Sep. 2013.

[30] X. Peng, J. Wang, S. Xiao, and W. Tang, "Strategies in covert communication with imperfect channel state information," in *Proc. IEEE Global Commun. Conf. (GLOBECOM)*, Dec. 2021, pp. 1–6.

[31] F. Haddadi, M. Malek-Mohammadi, M. M. Nayebi, and M. R. Aref, "Statistical performance analysis of MDL source enumeration in array processing," *IEEE Trans. Signal Process.*, vol. 58, no. 1, pp. 452–457, Jan. 2010.

[32] R. V. Hogg, J. McKean, and A. T. Craig, *Introduction to Mathematical Statistics*, 6th ed. London, U.K.: Pearson, Jun. 2004.
[33] I. M. Johnstone, "On the distribution of the largest eigenvalue in principal components analysis," *Ann. Stat.*, vol. 29, no. 2, pp. 295–327, Apr. 2001.
[34] H. F. Inman and E. L. Bradley Jr., "The overlapping coefficient as a measure of agreement between probability distributions and point estimation of the overlap of two normal densities," *Commun. Stat. Theory Methods*, vol. 18, no. 10, pp. 3851–3874, Mar. 1988.

SHUAIJUN MA received the B.S. degree in information and computing science from the University of Electronic Science and Technology of China, Chengdu, China, in 2022, where he is currently pursuing the M.E. degree with the National Key Laboratory of Science and Technology on Communications. His research interests include Internet-of-Things communications and backscatter communications.

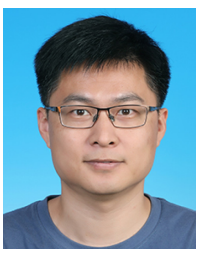

PENG WEI (Member, IEEE) received the Ph.D. degree in communication and information systems from the University of Electronic Science and Technology of China (UESTC) in 2017. From 2014 to 2016, he was a visiting student with the Department of Electrical and Computer Engineering, University of Delaware. From 2020 to 2023, he conducted postdoctoral research with the Department of Electronic Engineering, Tsinghua University. Since 2023, he has been an Associate Researcher with the National Key Laboratory of Wireless Communications, UESTC. His research interests are in wireless communications, multicarrier systems, anti-jamming communications, and signal processing.

SA XIAO received the B.S., M.S., and Ph.D. degrees from the University of Electronic Science and Technology of China, Chengdu, China, in 2009, 2012, and 2017, respectively. From February 2015 to August 2015, he was a visiting student with the Department of Electrical and Computer Engineering, Southern Illinois University, Carbondale, IL, USA. He also worked as a visiting student with the Division of Electrical and Computer Engineering, Louisiana State University, Baton Rouge, LA, USA, from August 2015 to February 2017. He is currently an Associate Professor with the National Key Laboratory of Science and Technology on Communications, University of Electronic Science and Technology of China. His research interests include covert communications, intelligent communications, and Internet-of-Things communications.

JIANQUAN WANG received the B.S. and Ph.D. degrees in communication and information system from the University of Electronic Science and Technology of China, Chengdu, China, in 2013 and 2019, respectively, where he is currently an Associate Professor. His research interests include security communications, information theory, and signal processing.

WANBIN TANG received the B.E., M.E., and Ph.D. degrees in electrical engineering from the University of Electronic Science and Technology of China (UESTC) in 1993, 1998, and 2013, respectively. From 2006 to 2007, he was a Visiting Scholar with the University of California at Berkeley, Berkeley, CA, USA. He is currently a Professor with the National Key Laboratory of Science and Technology on Communications, UESTC. His current research interests include cognitive radio and signal processing in wireless communication.

WEI XIANG (Senior Member, IEEE) is the Cisco Research Chair of AI and IoT and the Director of the Cisco-La Trobe Centre for AI and IoT, La Trobe University. Previously, he was the Foundation Chair and the Head of Discipline of IoT Engineering, James Cook University, Cairns, Australia. He has published over 300 peer-reviewed papers including three books and 220 journal articles. His research interest includes the Internet of Things (IoT), wireless communications, machine learning for IoT data analytics, and computer vision. Due to his instrumental leadership in establishing Australia's first accredited Internet of Things Engineering degree program, he was inducted into Pearcy Foundation's Hall of Fame in October 2018. He received the TNQ Innovation Award in 2016, and Pearcey Entrepreneurship Award in 2017, and Engineers Australia Cairns Engineer of the Year in 2017. He has been awarded several prestigious fellowship titles. He was a co-recipient of four Best Paper Awards at WiSATS'2019, WCSP'2015, IEEE WCNC'2011, and ICWMC'2009. He was named a Queensland International Fellow from 2010 to 2011 by the Queensland Government of Australia, an Endeavour Research Fellow from 2012 to 2013 by the Commonwealth Government of Australia, a Smart Futures Fellow from 2012 to 2015 by the Queensland Government of Australia, and a JSPS Invitational Fellow jointly by the Australian Academy of Science and Japanese Society for Promotion of Science from 2014 to 2015. He has served in a large number of international conferences in the capacity of the general co-chair, the TPC co-chair, and the symposium chair. He was the Vice Chair of the IEEE Northern Australia Section from 2016 to 2020. He is currently an Associate Editor of IEEE COMMUNICATIONS SURVEYS AND TUTORIALS, IEEE TRANSACTIONS ON VEHICULAR TECHNOLOGY, IEEE INTERNET OF THINGS JOURNAL, IEEE ACCESS, and *Scientific Reports* (Nature). He is a TEDx Speaker and an Elected Fellow of the IET in U.K., and Engineers Australia.